DOI: 10.26599/FSHW.2025.9250845

Contents lists available at SciOpen

Food Science and Human Wellness

journal homepage: https://www.sciopen.com/journal/2097-0765

China Food Publishing Co.

Nanoconfinement boosts electrochemiluminescence based on in-situ anchoring Pt NCs on mesoporous Mn_3O_4 for rapid and sensitive detection of *salmonella typhimurium*

Xiaobo Zhang[a], Xiuwen Wang[a], Longjiao Zhu[b], Jinyan Zhu[c,*], Bing Hu[a], Qiuyue Zheng[a], Jingli Yuan[a], Wentao Xu[b,*], Jijuan Cao[a,*]

[a] *Key Laboratory of Biotechnology and Bioresources Utilization of Ministry of Education, School of Life Sciences, Dalian Minzu University, Dalian, 116600, China*

[b] *Food Laboratory of Zhongyuan, Key Laboratory of Precision Nutrition and Food Quality, Department of Nutrition and Health, China Agricultural University, Beijing 100193, China*

[c] *Zhuanghe Food Inspection and Monitoring Center, Dalian, Liaoning Province, 116400, China*

ABSTRACT: The development of a simple, rapid and sensitive method for foodborne pathogens is essential to ensure public health safety. Existing methods, such as culture-based techniques and polymerase chain reaction (PCR), often face challenges in terms of time-consuming, labor-intensive, and require extensive sample preparation and amplification, which makes them impractical for rapid or on-site pathogen detection. Herein, a competitive mechanism-driven electrochemiluminescence (ECL) aptasensor was constructed for *Salmonella typhimurium* (*S. typhimurium*) detection without nucleic acid extraction and amplification. To boost the ECL signal of luminol-H_2O_2 systems, *in-situ* anchoring of Pt nanoclusters on mesoporous Mn_3O_4 nanoparticles (Pt NCs@M-Mn_3O_4) used as the nanoconfinement co-reactor. Benefitting from the restricted mesoporous structure, Pt NCs@M-Mn_3O_4 provided a unique microenvironment for the enrichment of H_2O_2. Furthermore, the interfacial interaction could activate the electronic transfer between active species of Pt NCs and M-Mn_3O_4, enabling a synergistic catalytic effect on ROS generation to effectively boost the ECL emission of luminol. The proposed ECL aptasensor had a linear concentration from 2×10^1 to 2×10^6 CFU/mL with limit of detection of 8 CFU/mL of *S. typhimurium*. Furthermore, the method showed high anti-interference ability. Especially, satisfactory recovery values in spiked-actual samples were obtained, thereby demonstrating great potential for sensitive and reliable detection of *S. typhimurium* in various environments.

Keywords: *electrochemiluminescence aptasensor, Salmonella typhimurium, nanoconfinement, mesoporous structure, Pt nanoclusters*

1. Introduction

Foodborne pathogens have become a serious threat to global public health. *Salmonella typhimurium* (*S. typhimurium*), is one of the most prevailing foodborne pathogens, which distributed in eggs, milk and meat[1-2]. The contaminated foods may cause various human foodborne disease, including abdominal cramp, fever, gastroenteritis, and even death[3]. Thus, it is of great significance to establish a sensitive and reliable

***Corresponding author**
caojijuan@dlnu.edu.cn; xuwentao@cau.edu.cn;
zhu40511516@163.com

Received 17 April 2025
Received in revised from 19 May 2025
Accepted 4 August 2025

detection method of *S. typhimurium* for food safety and public health[4]. The traditional detection methods for the detection of pathogenic bacteria included culture-based methods, polymerase chain reaction (PCR) and enzyme-linked immunosorbent assay (ELISA)[5-7]. Unfortunately, these methods suffer from limitations, such as long-time consumption, specialized instruments and requirement of highly skilled personnel[8-9]. In practical terms, there remains a need to develop a simple, fast and sensitive method for *S. typhimurium* detection.

The electrochemiluminescence (ECL) sensor that integrate electrochemistry and chemiluminescence together, has attracted great attentions as a powerful alternative because of its low background signal, wide dynamic response range, controllable reaction process and high sensitivity[10-11]. For the luminol-H_2O_2 binary system, an effective approach is regarding co-reaction accelerators to promote the decomposition of H_2O_2 into various reactive oxygen species (ROS) to enhance the ECL efficiency of luminol[12]. For example, Han and his colleagues employed horseradish peroxidase-modified gold nanorods (HRP/Au NRs) to catalyze H_2O_2 to acquire a high ECL signal intensity[13]. To overcome the signal decrease caused by vulnerable instability from natural enzymes, several co-reactant accelerators based nanomaterials, e.g., carbon material, transition-metal oxides and black phosphorus (BP), were prepared for promoting reduction of H_2O_2[14,15]. However, the nanozymes exposed their insufficient catalytic activity because active sites were wrapped inside the solid structure, severely limiting the improvement the ECL performance of luminol/H_2O_2 system[16]. Therefore, it is of great significance to develop a novel co-reactant accelerator to achieve the efficient generation of ROS for improving sensitivity and stability of ECL sensor.

Recently, platinum nanoclusters (Pt NCs), featured with excellent catalytic performance, good biocompatibility and easy to synthesis[17], have garnered considerable attention in the field of ECL sensing Analysis. Nevertheless, the catalytic activity of Pt NCs is often affected by the oxidation susceptibility and irreversible aggregation[18]. To address this issue, we synthesized flower-like mesoporous Mn_3O_4 nanoparticles (M-Mn_3O_4) with large surface area as confinement structures for anchoring and stabilization of Pt NCs. Compared with other confinement structures (e.g., metal-organic frameworks (MOFs)), the transition-metal oxides of M-Mn_3O_4 had more vacancies or defects, which remarkably improved the electrical and catalytic properties [19]. Besides, the vacancies or defects could act as a "claw" to anchor Pt NCs to avoid the migration of active Pt NCs. Herein, we compared the ECL efficiency of solid Mn_3O_4 (S-Mn_3O_4), M-Mn_3O_4 and Pt NCs@M-Mn_3O_4 to reveal the role of nanoconfinement in the enhancement of ECL signals. On the one hand, the mesoporous structure of Pt NCs@M-Mn_3O_4 had the higher specific surface area to improve the accessibility of a greater amount of H_2O_2, providing a restricted microenvironment for enrichment of H_2O_2[20]. On the other hand, the interfacial interaction could activate the electronic transfer between active species of Pt NCs and M-Mn_3O_4 support, which improved electrical conductivity and enabled a synergistic catalytic effect towards H_2O_2. Hence, the designed Pt NCs@M-Mn_3O_4 could employ as a novel nanoconfinement co-reaction accelerator to boost the luminol/H_2O_2 system for developing high performance sensor.

In this study, a simple, rapid and accurate sensor was constructed for *S. typhimurium* detection integrated with luminol/H_2O_2/Pt NCs@M-Mn_3O_4 ternary ECL system. The highly sensitive detection is realized based on target triggered the dissociation of double-stranded DNA (dsDNA) to switch ECL signal "off/on", without the additional operation of nucleic acid extraction and amplification. As shown in Scheme 1, benefiting from the nanoconfinement catalytic enhancement effect, the Pt NCs@M-Mn_3O_4 effectively accelerated the generation of ROS and produced a significantly enhanced ECL signal. Then, dopamine-modified *S. typhimurium* aptamer (DA-Apt) was used as quenching probe to anchor on the tetrahedral DNA nanostructures (TDNs) by hybridization with its complementary strand (cDNA). In the presence of target *S. typhimurium*, it was bound specifically by Apt, resulting in the release of quenching probe and recovery of the ECL emissions ("signal-on" state). The proposed competitive mechanism-driven ECL aptasensor for *S. typhimurium* detection exhibited a broad calibration curve range with good selectivity, reproducibility and stability. Furthermore, good feasibility of aptasensor was validated in actual milk samples, demonstrating a promising alternative for *S. typhimurium* analysis in food and environmental samples.

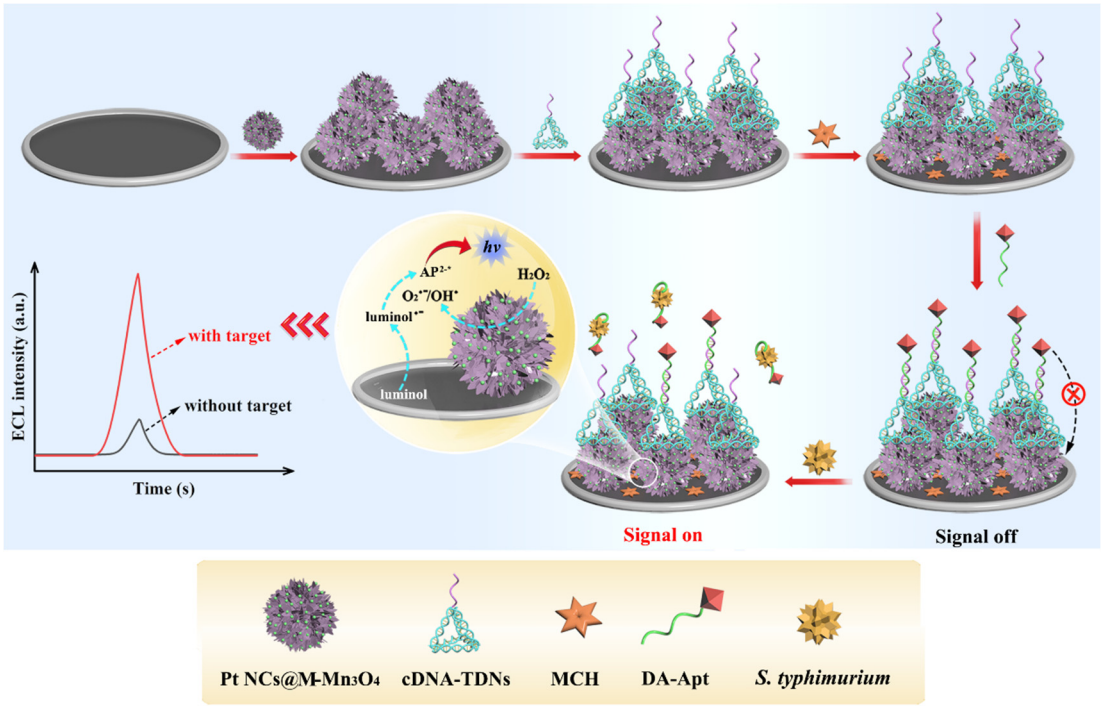

Scheme 1. Schematic illustration of a competitive mechanism-driven ECL aptasensor *for the detection of S. typhimurium* using Pt NCs@M-Mn_3O_4 as nanoconfinement co-reactor.

2. Experimental section

2.1. Reagents and apparatus

$KMnO_4$, $H_2PtCl_6 \cdot 6H_2O$ and $NaBH_4$ were purchased from Aladdin Chemical Co. Ltd. (Shanghai, China). The sequences of Apt of *S. typhimurium* (COOH-$(CH_2)_6$-TATGGCGGCGTCACCCGACGGGGACTTGACATTATGACAG) were synthesized by Sangon Biotech Co., Ltd. (Shanghai, China) and other sequence details for preparation of cDNA-TDNs is shown in Table S1. The bacteria used in this study were *S. typhimurium* (ATCC 14028), *Escherichia coli* (*E.*

coli, ATCC 25922), *Vibrio parahaemolyticus* (*V. parahaemolyticus*, ATCC 33847), *Listeria monocytogenes* (*L. monocytogenes*, ATCC 43251) and *Staphylococcus aureus* (*S. aureus*, ATCC 25923) were acquired Shanghai Luwei Technology Co., Ltd. The Supplementary Material (SM) provides information on other reagents and apparatus.

2.2 Synthesis of Pt NCs@M-Mn3O4

Pt NCs@M-Mn_3O_4 were synthesized using the *in-situ* deposition method[21]. 100 mg M-Mn_3O_4 sample was suspended in 30 mL of deionized water. Then, 0.5 mL of $H_2PtCl_6 \cdot 6H_2O$ solution (20 mmol/L) was added and sonicated for 30 min. Next, 3 mL of a solution containing $NaBH_4$ (0.1 M) and NaOH (0.2 M) was rapidly injected into the mixture and stirred for 1 h. Finally, centrifugation was used to separate the precipitate, which was then cleansed with deionized water and ethanol, and subsequently dried under a vacuum at 60℃ for 24 h to yield Pt NCs@M-Mn_3O_4. The synthesis details of S-Mn_3O_4, M-Mn_3O_4, bacterial culture, and cDNA-TDNs were described in the SM.

2.3 Construction and detection of the ECL aptasensor

The bare electrode was polished using Al_2O_3 polishing powder of 0.3 and 0.05 μm. Subsequently, the electrode surface was rinsed with ultrapure water and dried. Next, 6 μL of Pt NCs@M-Mn_3O_4 (2 mg/mL) solution was applied to create a uniform nanofilm on the electrode's surface. Following this, 6 μL of cDNA-TDNs (1 μM) were coated on the electrode interface via Pt-S bonds[22], acting as a scaffold to combine DA-Apt. Then, 6 μL of 6-mercaptohexanol (MCH) solution was added and incubated to block the nonspecific binding sites. Then, 6 μL of DA-Apt (1.5 μM) was introduced to the electrode surface to generate dsDNA via DNA hybridization. Finally, to remove uncombined biomolecules, the modified electrode was rinsed with PBS and was stored at 4 ℃ for subsequent use. The optimization of concentration of Pt NCs@M-Mn_3O_4 and DA-Apt were shown in Fig S1.

For *S. typhimurium* detection, a solution with varying concentrations from 2×10^1 to 2×10^6 CFU/mL was added to the modified electrode using 6 μL of the *S. typhimurium* solution and incubated for 40 min. After washing with PBS, the ECL intensity of aptasensor was recorded in 5 mL PBS (pH 7.4) solution containing 10 μmol/L luminol and 1.0 mmol/L H_2O_2 by using an ECL detector under scan potentials scan from 0 to 0.6 V at a rate of 50 mV/s, with operated voltage of 600 V.

2.4 Preparation and detection of S. typhimurium in actual samples

Milk, chicken meat and lettuce samples were purchased from a Walmart Supermarket in Dalian. First, all samples were irradiated and determined by culture-based method that *S. typhimurium* was not present. Then, the milk samples were centrifuged to obtain the supernatant. The chicken and lettuce samples were cut into pieces and homogenized with 10 mL PBS solution, and then filtered after centrifugation to obtain the supernatant. The supernatant was diluted 10 times with PBS to serve as the milk, chicken meat and lettuce samples solutions. Subsequently, different concentrations of *S. typhimurium* were mixed with the above samples to acquire a final concentration of 1.52×10^2, 1.52×10^4 and 1.52×10^5 CFU/ mL, respectively.

Finally, *S. typhimurium* analysis in milk, chicken meat and lettuce samples were carried out with the established ECL aptasensor.

3. Results and discussion

3.1. Principle of the ECL aptasensor

Scheme 1 illustrated the fabrication process and a competitive mechanism-driven ECL sensing principle for detecting *S. typhimurium*. Initially, the prepared Pt NCs@M-Mn_3O_4 provided a nanoconfinement catalytic enhancement effect on the luminol/H_2O_2 system, leading to an amplified ECL signal. Following the introduction of DA-Apt to the sensing interface through DNA hybridization, the ECL signal was quenched, resulting in the "signal off" state. Upon the presence of *S. typhimurium* in the system, it specifically bound to DA-Apt, causing detachment of quenching probe from the electrode surface. This detachment recovered the ECL signal and switched the "signal on" state. By monitoring the ECL signal intensity, the *S. typhimurium* concentration could be quantified free of nucleic acid extraction and amplification.

3.2. Characterization of cDNA-TDNs and binding of the Apt with the target

The synthesized cDNA-TDNs were characterized via agarose gel electrophoresis (Fig S2). Results showed lane 4 (TDN-a+b+c+d) had the slower migration compared to lanes 1 (TDN-a), 2 (TDN-a+b), and 3 (TDN-a+b+c), due to its three-dimensional structure and large molecular weight, indicating successful assembly of cDNA-TDNs [23]. Lane 5 showed the slowest electrophoretic migration rate owing to a further increase in molecular weight, when Apt hybridized with cDNA-TDNs successfully. In the presence of the target *S. typhimurium*, it specifically bound to Apt and triggered the release of Apt, and lane 6 exhibited a distinct shift in migration and was in the same position as lane 4. These results demonstrated that the designed sequences are feasible to detect *S. typhimurium*.

3.3. Morphology and structure characterization of prepared nanomaterials

The Pt NCs@M-Mn_3O_4 composites was synthesized using hydrothermal synthesis, carbonization and *in-situ* deposition methods, as illustrated in Fig. 1A. In addition, the S-Mn_3O_4 and M-Mn_3O_4 were prepared as control materials. The XRD provided insights into the structure and phase composition of obtained S-Mn_3O_4, M-Mn_3O_4 and Pt NCs@M-Mn_3O_4. In Fig. S3, the XRD of S-Mn_3O_4 showed that strong diffraction peaks at 18.0°, 28.9°, 32.4°, 36.1°, 44.5°, 59.9° and 64.8°, corresponded to the (101), (112), (103), (211), (220), (224) and (400) planes of hausmannite tetragonal crystal of Mn_3O_4 (PDF#24-0734), respectively[24]. For M-Mn_3O_4 sample (Fig. 1B), the characteristic peaks agreed with the S-Mn_3O_4, indicating morphology changes had no effect on the phase composition. After anchoring of Pt NCs on M-Mn_3O_4, a weak and broad diffraction peak at 39.6° assigned to (111) plane of face-centered cubic Pt (PDF#04-0802) was observed[25], which was attributed to the high dispersion and ultrasmall size of Pt NCs.

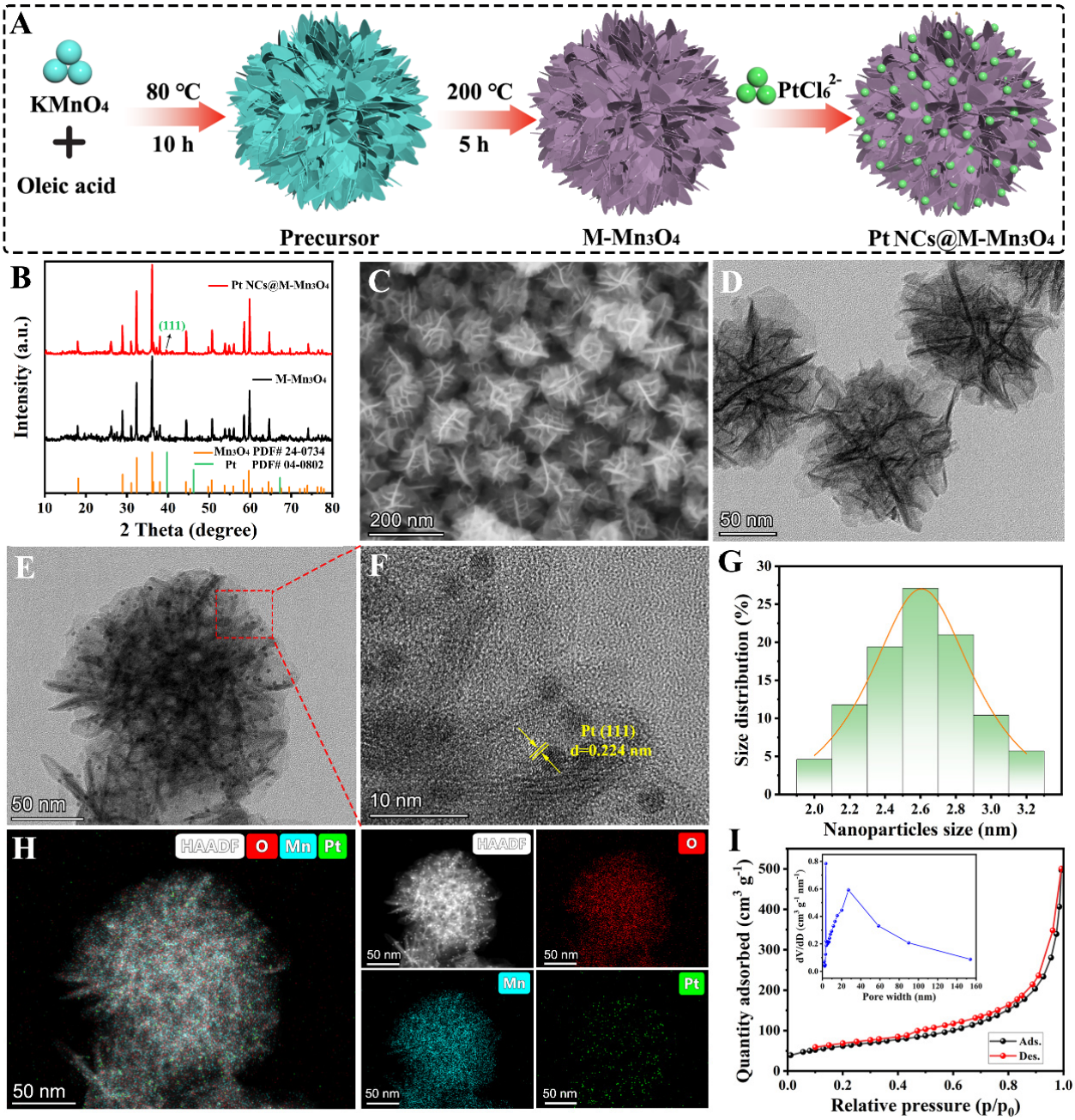

Fig. 1. (A) Schematic illustration of synthetic process of Pt NCs@M-Mn_3O_4 composite. (B) XRD patterns of M-Mn_3O_4 and Pt NCs@M-Mn_3O_4. (C) SEM and (D)TEM image of M-Mn_3O_4. (E) TEM and (F) HRTEM image of Pt NCs@M-Mn_3O_4. (G) The measured size distribution of Pt NCs. (H) EDS elemental mapping Pt NCs@M-Mn_3O_4. (I) N_2 adsorption and desorption measurements of Pt NCs@M-Mn_3O_4.

In addition, the surface morphology of prepared nanomaterials was characterized by SEM and TEM technologies. As shown in Fig. 1C and 1D, the of M-Mn_3O_4 had the flower-like structure with particles size in 100-130 nm. Compared with S-Mn_3O_4 (Fig. S4), the M-Mn_3O_4 could expose more catalytic active sites for reduction of H_2O_2. Besides, it could offer the accessible hollow microchannel, which facilitated the loading of Pt NCs to a greater extent. In Fig. 1E, after the M-Mn_3O_4 was used as a supporting substrate to capture Pt NCs, the M-Mn_3O_4 still kept the flower-like structure and a large number of Pt NCs with monodisperse and uniform sizes (an average diameter of 2.6 nm) were decorated on M-Mn_3O_4 (Fig. 1G). In Fig. 1F, the high-resolution TEM of Pt NCs@M-Mn_3O_4 further revealed that the interplanar spacing of 0.224 nm were attributed to the (111) facets of Pt[26]. To further investigate the elemental distribution, the energy spectrometry (EDS)

elemental mapping images of Pt NCs@M-Mn_3O_4 was shown in Fig. 1H. These images confirmed the uniform distribution of Pt NCs on M-Mn_3O_4, suggesting successful preparation of Pt NCs@M-Mn_3O_4 through the *in-situ* deposition strategy. Furthermore, Pt NCs@M-Mn_3O_4 modified electrode was characterized through SEM image (Fig. S5B), it revealed that Pt NCs@M-Mn_3O_4 nanocomposites were homogeneously immobilized on the electrode surface, ensuring the feasibility for subsequent sensor assembly. In Fig. 1I, the Brunauer-Emmett-Teller (BET) specific surface area of Pt NCs@M-Mn_3O_4 is 223.2 m^2/g with an average pore size of 14.4 nm based on N_2 adsorption and desorption measurements, while that of the pure M-Mn_3O_4 material was 182.7 m^2/g (Fig. S6). The increased specific surface area is attributed to the high dispersion and ultrasmall size of Pt NCs. Therefore, the Pt NCs@M-Mn_3O_4 exhibited the higher specific surface area and accessible mesoporous structure, which provided more catalytic active sites and accommodates more luminol/H_2O_2 substrates.

As illustrated in Fig. 2, the elemental composition and chemical states of Pt NCs@M-Mn_3O_4 were further investigated via XPS characterization. The full spectrum XPS (Fig. 2A) presented several characteristic peaks at binding energies of 71.5 eV, 284.8 eV, 531.3 eV, and 641.7 eV, corresponding to Pt 4f, C 1s, O 1s, and Mn 2p, respectively, which was consistent with EDS dates. The high-resolution XPS spectrum of the Mn 2p is exhibited in Fig. 2B, two prominent peaks located at 641.7 and 653.4 eV attributed to Mn $2p_{3/2}$ and Mn $2p_{1/2}$ of M-Mn_3O_4[27]. In addition, the O 1s spectrum (Fig. 2C) could be deconvoluted into three peaks at binding energies of 529.7, 531.0 eV and 531.9 eV corresponded to metal-oxygen (M-O) bond, surface oxygen defects (O_d) and surface adsorbed oxygen (O_a), respectively[28]. For the high-resolution Pt 4f spectrum (Fig. 2D), two peaks at 71.5 and 74.6 eV belonged to Pt $4f_{7/2}$ and Pt $4f_{5/2}$, respectively[29]. The above results adequately confirmed the successful synthesis of Pt NCs@M-Mn_3O_4.

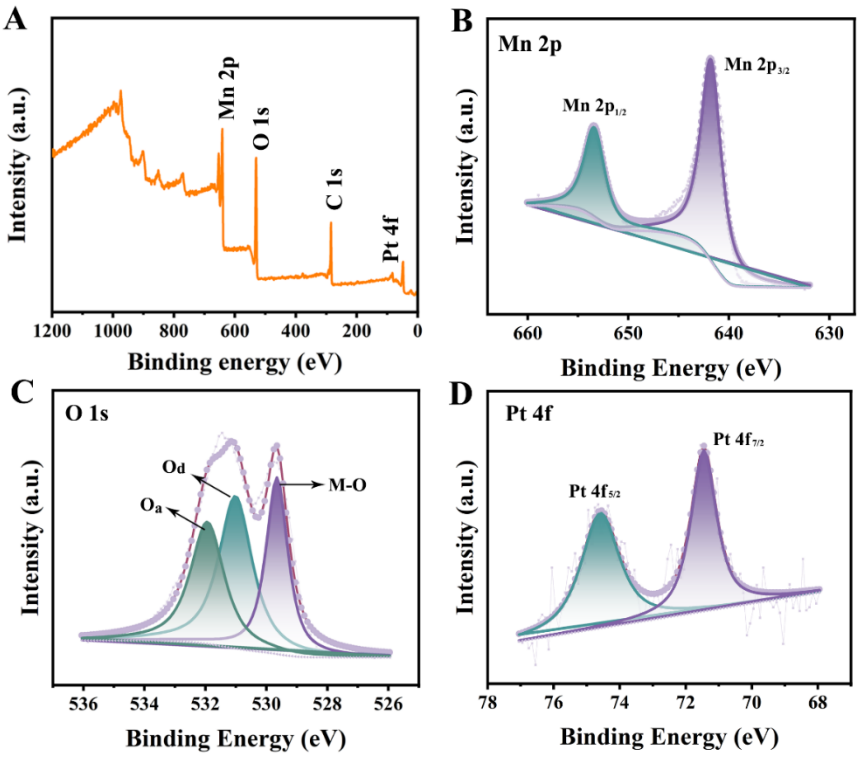

Fig. 2. (A) XPS analysis of the full region of Pt NCs@M-Mn_3O_4. (B) Spectra of Mn 2p and (C) O 1s (D) Pt 4f.

3.4. Electrochemical characterization of Pt NCs@M-Mn3O4

Fig 3A displays the electrochemical behavior of GCE modified with different materials, as investigated by electrochemical impedance spectroscopy (EIS)[30]. The diameter of the semicircle represents the charge transfer resistance (R_{et}), which is influenced by the modification of the electrode surface[31]. The electron transfer resistance (R_{et}) value of the Pt NCs@M-Mn_3O_4/GCE was lower than those of M-Mn_3O_4/GCE and S-Mn_3O_4/GCE. Two possible reasons of enhanced interfacial electron transfer are as follows: (i) the M-Mn_3O_4 with mesoporous structure provided accessible microchannel for electroactive $Fe(CN)_6]^{3-/4-}$. (ii) the interfacial interaction could activate the electronic transfer between active species of Pt NCs and M-Mn_3O_4. To characterize the effective electroactive surface area of Pt NCs@M-Mn_3O_4, CV were recorded at different scan rates (0.01-0.2 V/s). The electroactive surface area was calculated using the Randles-Sevcik equation[32]: $I_p = (2.69 \times 10^5) AD^{1/2}n^{3/2}v^{1/2}c$, where I_p is the peak reduction current, A is the effective electroactive surface area of the electrode, D is the diffusion coefficient of $K_3[Fe(CN)_6]$ (6.7×10^{-6} cm²/s), *n* is the number of electrons involved in the reaction (n = 1), *v* is the scan rate (V/s) and *c* is the volume concentration of $K_3[Fe(CN)_6]$ (5 mmol/L). Correspondingly, electroactive surface area of Pt NCs@M-Mn_3O_4 was calculated to be 0.11 cm² (Fig 3B), significantly larger than those of M-Mn_3O_4 (0.08 cm², Fig S7A) and S-Mn_3O_4 (0.06 cm², Fig S7B).

To investigate the ECL emission of luminol-H_2O_2 system under different material, ECL intensity-potential curves of electrodes modified with Pt NCs@M-Mn_3O_4, M-Mn_3O_4 and S-Mn_3O_4 were recorded in PBS (pH 7.4), respectively. In Fig 3C, the ECL signal of bare GCE is inferior. Obviously, the Pt NCs@M-Mn_3O_4-modified electrode exhibited a negatively shifted anodic potential and an enhanced electrical oxidation peak of luminol comparing with M-Mn_3O_4 and S-Mn_3O_4. The synergistic effect of different active species from Pt NCs@M-Mn_3O_4 resulted in a high catalytic performance to facilitate the conversion efficiency of H_2O_2 into ROS. Additionally, the mesoporous structure of Pt NCs@M-Mn_3O_4 improved the accessibility of a greater amount of H_2O_2, which offered the nanoconfinement effect for the reaction between luminol and ROS, leading to a significant enhancement in luminol emission. Next, the ECL-time curves were studied and the results were shown in Fig 3D. The Pt NCs@M-Mn_3O_4 exhibited the maximum ECL intensity (15731 a.u.), which was 1.45-fold and 3.42-fold higher than the M-Mn_3O_4 and S-Mn_3O_4, respectively, confirming that Pt NCs@M-Mn_3O_4 could act as a nanoconfined co-reacting accelerator in luminol-H_2O_2 system.

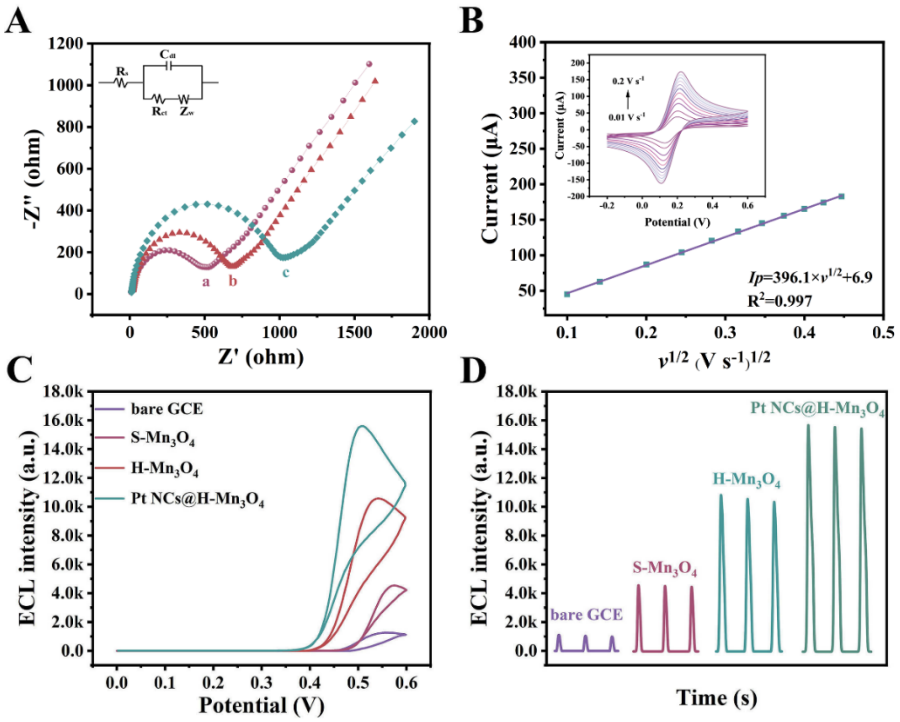

Fig. 3. (A) EIS plots of (a) Pt NCs@M-Mn_3O_4/GCE, (b) M-Mn_3O_4/GCE, (c) S-Mn_3O_4/GCE (EIS test in the PBS containing 5 mmol/L $[Fe(CN)_6]^{3-/4-}$ containing 0.1 mol/L KCl). (B) Linear relation between the reduction peak current I_p and $v^{1/2}$ (inset: CV curves of Pt NCs@M-Mn_3O_4 at scan rates of 0.01-0.2 V/s). (C) ECL-potential profiles and (D) ECL-time profiles of different materials-modified electrodes.

To investigate the enhancement mechanism of the ECL signal by Pt NCs@M-Mn_3O_4, Fig S8 demonstrated that when Pt NCs@M-Mn_3O_4/GCE containing luminol or bare GCE containing luminol and H_2O_2 only had the low ECL signals. However, ECL emission of ternary luminol-H_2O_2-Pt NCs@M-Mn_3O_4 system was significantly enhanced, confirmed that Pt NCs@M-Mn_3O_4 could effectively facilitate the conversion efficiency of H_2O_2 into ROS to boost ECL signal of luminol. To elucidate the types of ROS in the ternary luminol-H_2O_2-Pt NCs@M-Mn_3O_4 system, different types of radical scavengers were introduced into the system, including benzoquinone (BQ, $O_2^{\bullet-}$ scavenger) and isopropyl alcohol (IPA, $OH^{\bullet}$ scavenger). ECL signal was significantly reduced by 89.4 % upon the addition of IPA, as depicted in Fig S9. Meanwhile, BQ at equal concentration quenched the ECL emission by 35.2 %. Overall, the above results implied that the $OH^{\bullet}$ plays a dominant role in the enhancement of the ECL signal.

Furthermore, the possible ECL mechanism of Pt NCs@M-Mn_3O_4-assisted luminol-H_2O_2 system is as illustrated in Fig S10. First, the Pt NCs@M-Mn_3O_4 catalyzed the conversion of H_2O_2 into ROS ($OH^{\bullet}$ and $O_2^{\bullet-}$). Meanwhile, luminol anionic radicals ($luminol^{\bullet-}$) was produced from the electrochemical oxidation of luminol anions ($luminol^{-}$)under the action of a positive potential, then the $luminol^{-}$ reacted with the more ROS to generate excited state 3-aminophthalate anion (AP^{2-*}). As AP^{2-*} returned to its ground state, ultimately leading to a strong ECL emission.

3.5. Characterization and feasibility of the constructed ECL aptaosensor

The stepwise fabrication process of the aptasensor was elucidated through EIS characterization[33]. As illustrated in Fig. 4A, the bare GCE had a small semicircle (curve a). Upon modification with Pt

NCs@M-Mn_3O_4, a slight increase in R_{et} was observed (curve b). Subsequent immobilization of the cDNA-TDNs, the R_{et} increased because negatively charged phosphate group of cDNA-TDNs repelled the $[Fe(CN)_6]^{3-/4-}$ (curve c). After modifying with MCH (curve d) and DA-Apt (curve e), the Ret reached its maximum value, which could be attributed to the fact that increased steric hindrance inhibited the electron transport. Simultaneously, the ECL behavior of the electrodes were monitored during the sensor fabrication process. As depicted in Fig. 4B, the Pt NCs@M-Mn_3O_4/GCE exhibited the highest ECL intensity (curve b, 15819 a.u.), reflecting the excellent catalytic activity of the Pt NCs@M-Mn_3O_4 toward luminol-H_2O_2 system. However, after incubation with cDNA-TDNs (curve c, 13366 a.u.) and MCH (curve d, 11790 a.u.), the ECL intensity decreased due to electron transfer obstruction by these insulating substances[34]. Notably, upon hybridization with DA-Apt, the ECL intensity diminished by 82.8% (curve e, 2027 a.u.), likely because DA acted as an effective ECL signal quencher. In brief, the changes of EIS and ECL-time curves indicated the successful fabrication of the ECL aptasensor.

Furthermore, the feasibility of the designed ECL aptasensor was validated selecting *S. typhimurium* at a concentration of 2×10^5 CFU/mL. As exhibited in Fig 4C, at the absence of *S. typhimurium,* the ECL signal of aptasensor was in "signal off" state (2027 a.u.) due to the quenching effect of DA on the luminol emission. When *S. typhimurium* was added into the detection system, it specifically bound its Apt and triggered the detachment of dsDNA to release DA, leading to the recovery of the ECL response ("signal on" state, 8454 a.u.). The above results suggested that the "signal off/on" ECL sensor had good feasibility for detecting *S. typhimurium*.

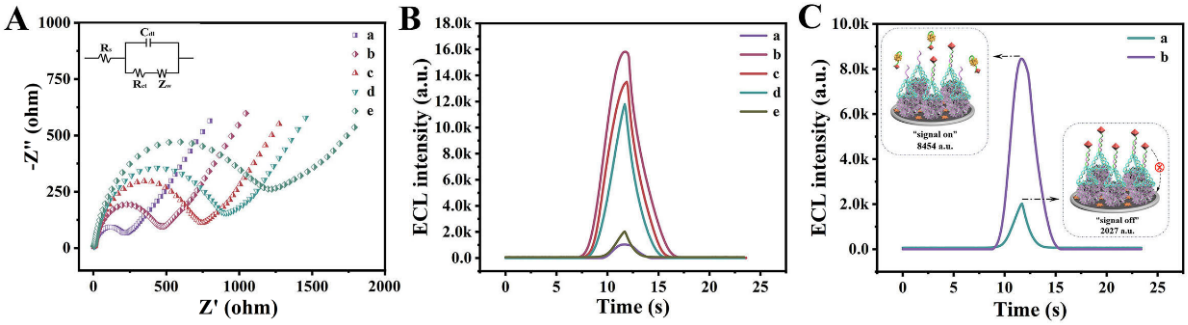

Fig. 4. (A) EIS plots and (B) ECL-time profiles of assembly process of aptasensor: (a) bare GCE, (b) GCE/Pt NCs@M-Mn_3O_4, (c) GCE/Pt NCs@M-Mn_3O_4/cDNA-TDNs, (d) GCE/Pt NCs@M-Mn_3O_4/cDNA-TDNs/MCH, (e) GCE/Pt NCs@M-Mn_3O_4/cDNA-TDNs/MCH/DA-Apt. (C) ECL feasibility of the proposed sensing system in the absence and presence of 2×10^5 CFU/mL target.

3.6. Detection of S. typhimurium the ECL sensing platform

Under the optimal conditions (pH 7.4 and incubation of *S. typhimurium* 40 min, the detailed information in Fig. S11), the proposed ECL sensor was used for precise quantification of the *S. typhimurium* at various levels. ECL intensity-time curves of Fig 5A displayed the ECL signal intensity increased with higher concentrations of *S. typhimurium* (2×10^1-2×10^6 CFU/mL). In Fig 5B, a linear equation was expressed as I_{ECL}=1546.63 LgC+121.52 (R^2=0.995) with a limit of detection (LOD) of 8 CFU/mL based on ECL intensity against the logarithm of the *S. typhimurium* concentration. In addition, the proposed sensing platform was

compared with the reported *S. typhimurium* analysis methods, showing satisfactory performance in terms of LOD, linear detection range and cost (Table S2 and Table S3).

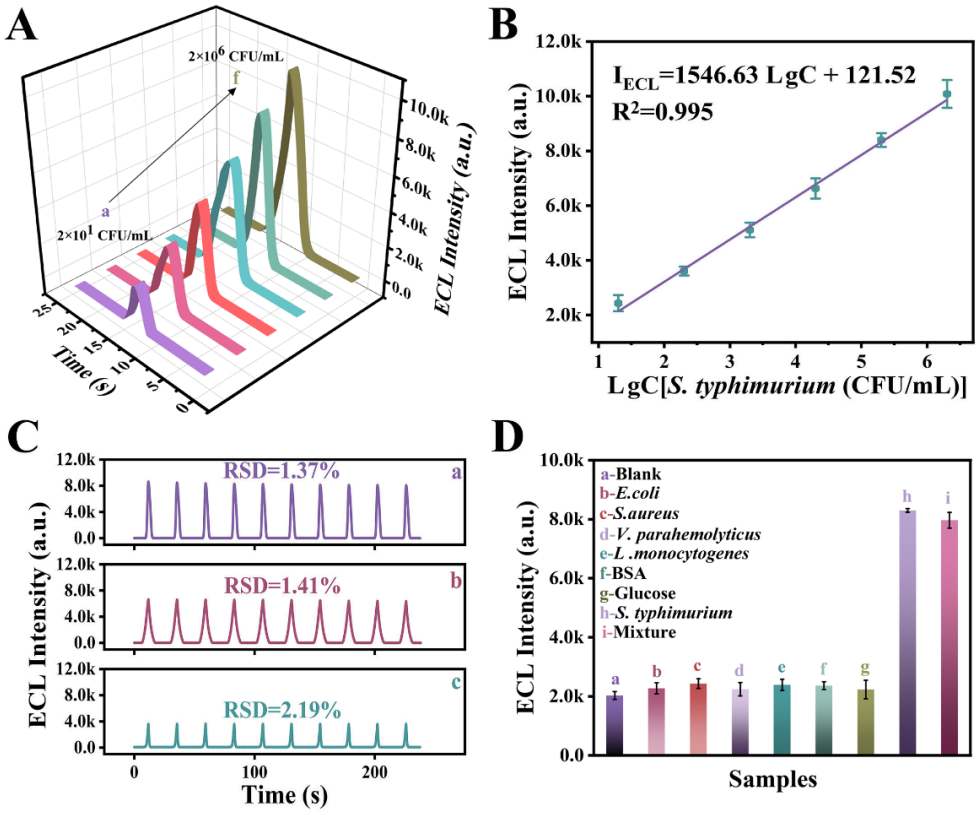

Fig. 5. (A) ECL intensity corresponding to different concentrations of *S. typhimurium*. (B) Linear relationship between the logarithm of different concentrations of *S. typhimurium* and the corresponding ECL intensity. (C) Signal stability of the ECL sensor with different concentrations under the continuous scanning of 10 cycles: (a) 2×10^5 CFU/mL (b) 2×10^4 CFU/mL (c) 2×10^2 CFU/mL. (D) Selectivity of the proposed ECL aptasensor.

3.7. Stability, reproducibility, and selectivity of ECL sensor

The operational stability of the sensor was evaluated by conducting 10 continuous cyclic potential scans at concentrations of 2×10^2, 2×10^4, and 2×10^5 CFU/mL of *S. typhimurium* (Fig. 5C). The resulting RSD values were 1.37%, 1.41%, and 2.19%, respectively, indicating highly consistent ECL responses across multiple cycles. In addition, storage stability was investigated by ECL signal change of sensor over a 20 days period. As seen in Fig. S12, the signal maintained 92.64% of the initial value after 20 days. These results underscore the excellent stability of sensor, because that M-Mn_3O_4 effectively prevents the agglomeration of Pt NCs and provides the stable and drift-free ECL signal. To explore the reproducibility of this sensor, five identical sets of sensors under consistent reaction conditions were further tested. In Fig. S13, the relative standard deviations (RSDs) were less than 2.40%, demonstrating the sensor's acceptable reproducibility. Given the complexity of the actual sample and detection environment, the selectivity of sensing system was assessed by introducing various substances, including *E. coli*, *S. aureus*, *V. parahemolyticus*, *L. monocytogenes,* BSA, and glucose (Fig. 5D). The results indicated that the influence of these interfering substances was negligible and the ECL system was in "signal off" state. Only the *S. typhimurium* and mixed samples (2×10^5 CFU/mL of *S. typhimurium* +2×10^6 CFU/mL of interferent) could trigger "signal on" state. Consequently, we confirmed that the sensor has satisfactory selectivity for the *S. typhimurium* assay.

3.8. Detection of S. typhimurium in actual samples

To further validate the applicability and feasibility of ECL assay in detecting *S. typhimurium* in actual samples were spiked with various levels of bacteria (1.52×10^2, 1.52×10^4 and 1.52×10^5 CFU/mL). As listed in Table S4, the recovery values ranged from 95.4% to 102.6% with RSD of less than 4.18%. Furthermore, the designed ECL aptasensor showed good agreement with standard ELISA method (relative errors within ± 5.4%), which suggested its acceptable anti-interference capability in complex food matrices, holding a good reliability for *S. typhimurium* detection in practical situations.

4. Conclusions

In this work, we synthesized Pt NCs@M-Mn_3O_4 through *in-situ* deposition method and employ it as an efficient nanoconfinement co-reactor in luminol-H_2O_2 system. The Pt NCs@M-Mn_3O_4 exhibited unique mesoporous structure, large electroactive area and excellent catalytic activity, which could promote interfacial electron transfer and the generation of ROS, leading to the enhancement of ECL efficiency of luminol. Initially, DA-Apta was used as quenching probe to inhibit the ECL signal ("signal off" state). Upon specific recognition of *S. typhimurium* by its Apt, the target initiated the competitive displacement reaction, resulting in "signal on" state. The resulting ECL sensor achieved highly sensitive detection for *S. typhimurium* free of nucleic acid extraction and amplification, with a low LOD of 8 CFU/mL. As expected, the satisfactory practical applicability in actual samples. The sensing platform integrated Pt NCs@M-Mn_3O_4 with competitive sensing mechanism could provide new prospects for other pathogens detection, pushing forward the high-performance ECL bioassay.

Declaration of interests

The authors declare that they have no known competing financial interests or personal relationships that could have appeared to influence the work reported in this paper.

Acknowledgments

This work was supported by the National Key Research and Development Program of China (2024YFF1105803), National Natural Science Foundation of China (32402226), Applied Basic Research Program of Liaoning Province (2023JH2/101700030), Science and Technology Project for Distinguished Young Scholars of Dalian (2023RJ003), Science and Technology Project for Outstanding Young Scholars of Dalian (2024RY026) and Fundamental Research Funds for the Central Universities (044420250051).

References

[1] J. Chen, Z. Huang, Z. Luo, et al., Multichannel-Structured Three-Dimensional Chip for Highly Sensitive Pathogenic Bacteria Detection Based on Fast DNA-Programmed Signal Polymerization, Anal. Chem. 90 (2018) 12019-12026. https://doi.org/10.1021/acs.analchem.8b02650.

[2] L. Zheng, G. Cai, W. Qi, et al., Optical biosensor for rapid detection of Salmonella typhimurium based on porous gold@ platinum nanocatalysts and a 3D fluidic chip, ACS sensors 5 (2019) 65-72. https://doi.org/10.1021/acssensors.9b01472.

[3] L. Gong, J. Liang, Y. Zhang, et al., An antifouling electrochemical biosensor using self-signal for Salmonella typhimurium direct detection in food sample, Food Chem. 452 (2024) 139536. https://doi.org/10.1016/j.foodchem.2024.139536.

[4] M. Yan, H. Li, M. Li, et al., Advances in surface-enhanced Raman scattering-based aptasensors for food safety detection, J. Agric. Food Chem. 69 (2021) 14049-14064. https://doi.org/10.1021/acs.jafc.1c05274.

[5] L. Jiang, B. Zhang, S. Liu, et al., The MBS microbial rapid detection system for rapid detection of major pathogenic bacteria in feed: comparison with plate counting method, BMC Microbiol. 22 (2022) 242. https://doi.org/10.1002/smll.202306473.

[6] R. Gao, X. Liu, Z. Xiong, et al., Research progress on detection of foodborne pathogens: The more rapid and accurate answer to food safety, Food Res. Int. (2024) 114767. https://doi.org/10.1016/j.foodres.2024.114767.

[7] B. Guo, Y. Zhao, C. Zhou, et al., The detection of Salmonella in food based on PCR combined with Pyrococcus furiosus Argonaute, Microchem. J. (2024) 111311. https://doi.org/10.1016/j.microc.2024.111311.

[8] W. Peng, Y. Liu, M. Lu, et al., Advances in surface-enhanced Raman scattering detection of foodborne pathogens: From recognition-based fingerprint to molecular diagnosis, Coord. Chem. Rev. 518 (2024) 216083. https://doi.org/10.1016/j.ccr.2024.216083.

[9] R. Sivakumar, N.Y. Lee. Advances in deoxyribonucleic acid extraction techniques and point-of-care molecular diagnosis of foodborne pathogens, Analyst. 148 (2023) 3153-3168. https://doi.org/10.1039/D3AN00045A.

[10] J. Liu, Y. Shen, G. Wang, et al., Highly-sensitive electrochemiluminescence biosensor for detection of inosine monophosphate in meat based on graphdiyne/AuNPs/luminol nanocomposites, Food Sci Hum Well. 12 (2023)1149-1156. https://doi.org/10.1016/j.fshw.2022.10.040.

[11] H. Xu, C. Li, R. Mao, et al., Colorimetric and ECL dual-mode aptasensor for smartphone-based onsite sensitive detection of aflatoxin B1 in combination with ZnO@ MWCNTs/g-C3N4 nanosheets and CuO@ CuPt nanocomposites, Biosens. Bioelectron. 262 (2024) 116569. https://doi.org/10.1016/j.bios.2024.116569.

[12] W. Gu, H. Wang, L. Jiao, et al., Single-atom iron boosts electrochemiluminescence, Angew. Chem. 132 (2020) 3562-3566. https://doi.org/10.1002/ange.201914643.

[13] L. Wu, F. Ding, W. Yin, et al., From electrochemistry to electroluminescence: development and application in a ratiometric aptasensor for aflatoxin B1, Anal. Chem. 89 (2017) 7578-7585. https://doi.org/10.1021/acs.analchem.7b01399.

[14] L. Hu, Y. Wu, M. Xu, et al., Recent advances in co-reaction accelerators for sensitive electrochemiluminescence analysis, Chem. Commun. 56 (2020) 10989-10999. https://doi.org/10.1039/D0CC04371K.

[15] X. Ren, M. Shao, Z. Xie, et al., A Co-Reactive Immunosensor Based on Ti3C2T x MXene@ TiO2–MoS2 Hybrids Promoting luminol@ Au@ Ni–Co NCs Electrochemiluminescence for CYFRA 21–1 Detection, ACS sensors. 9 (2024) 1992-1999. https://doi.org/10.1021/acssensors.3c02784.

[16] J.-H. Li, J.-L. Liu, X.-L. Zhang, et al., Ultrasensitive electrochemiluminescence biosensor based on 2D Co3O4 nanosheets as a coreaction accelerator and highly ordered rolling DNA nanomachine as a signal amplifier for the detection of microRNA, Anal. Chem. 95 (2023) 4131-4137. https://doi.org/10.1021/acs.analchem.2c05116.

[17] Y. Li, X. Jian, S. Zhou, et al., Protein shell-encapsulated Pt clusters as continuous O2-supplied biocoats for photodynamic therapy in hypoxic cancer cells, ACS Appl. Mater. Interfaces. 11 (2019) 17215-17225. https://doi.org/10.1021/acsami.9b02484.

[18] S. Tian, J. Li, D. Xiao, et al., Self-Enhanced Catalytic Activity of Pt/TiO2 via Electronic Metal–Support Interaction, ACS Cent. Sci. 9 (2023) 7-9. https://doi.org/10.1021/acscentsci.2c01546.

[19] Y. Du, J. Xue, X. Sun, et al., Oxygen vacancy-enhanced electrochemiluminescence sensing strategy using luminol thermally encapsulated in apoferritin as a transducer for biomarker immunoassay, Anal. Chem. 92 (2020) 8472-8479. https://doi.org/10.1021/acs.analchem.0c01238.

[20] Y. Han, X. Ren, T. Wu, et al., Wu, Effective Enrichment of Free Radicals through Nanoconfinement Boosts Electrochemiluminescence of Carbon Dots Derived from Luminol, Angew. Chem. 137 (2024) e202414073. https://doi.org/10.1002/ange.202414073.

[21] Y. Wang, C. Jiang, Y. Le, et al., Hierarchical honeycomb-like Pt/NiFe-LDH/rGO nanocomposite with excellent formaldehyde decomposition activity, Chem. Eng. J. 365 (2019) 378-388. https://doi.org/10.1016/j.cej.2019.01.187.

[22] Z. Qing, G. Luo, S. Xing, et al., Pt–S Bond-Mediated Nanoflares for High-Fidelity Intracellular Applications by Avoiding Thiol Cleavage, Angew. Chem. Int. Ed. 59 (2020) 14044-14048. https://doi.org/10.1002/anie.202003964.

[23] C. Hong, X. Zhang, S. Ye, et al., Aptamer-pendant DNA tetrahedron nanostructure probe for ultrasensitive detection of tetracycline by coupling target-triggered rolling circle amplification, ACS Appl. Mater. Interfaces 13 (2021) 19695-19700. https://doi.org/10.1021/acsami.1c02612.

[24] Y. Li, H. Tan, X.-Y. Yang, et al., Well Shaped Mn3O4 Nano-octahedra with Anomalous Magnetic Behavior and Enhanced Photodecomposition Properties, Small 7 (2011) 475-483. https://doi.org/10.1002/smll.201001403.

[25] H. Huang, Y. Chen, J. Zuo, et al., MXene-incorporated C60NPs and Au@ Pt with dual-electric signal outputs for accurate detection of Mycobacterium tuberculosis ESAT-6 antigen, Biosens.Bioelectron. 242 (2023) 115734. https://doi.org/10.1016/j.bios.2023.115734.

[26] F. Guo, Y.-P. Wei, S.-Q. Wang, et al.,Pt nanoparticles embedded in flowerlike NH 2-UiO-68 for enhanced photocatalytic carbon dioxide reduction, J. Mater. Chem. A, 7 (2019) 26490-26495. https://doi.org/10.1039/C9TA10575A.

[27] N. Singh, M.A. Savanur, S. Srivastava, et al., A redox modulatory Mn3O4 nanozyme with multi-enzyme activity provides efficient cytoprotection to human cells in a Parkinson's disease model, Angew. Chem. 129 (2017) 14455-14459. https://doi.org/10.1002/ange.201708573.

[28] X. Lin, S. Li, H. He, et al., Evolution of oxygen vacancies in MnOx-CeO2 mixed oxides for soot oxidation, Appl Catal B-Environ 223 (2018) 91-102. https://doi.org/10.1016/j.apcatb.2017.06.071.

[29] J. Wang, J. Wu, M. Sun, et al., Pt nanoparticles/laser-engraved graphene-based integrated electrochemical platform for point-of-use determination of ponceau 4R, amaranth and tartrazine in food, Food Chem. 435 (2024) 137611. https://doi.org/10.1016/j.foodchem.2023.137611.

[30] X. Zhang, Z. Li, L. Yang, et al., CRISPR/Cas12a-Derived Photoelectrochemical Aptasensor Based on Au Nanoparticle-Attached CdS/UiO-66-NH2 Heterostructures for the Rapid and Sensitive Detection of Ochratoxin A, J. Agric. Food Chem. 72 (2023) 874-882. https://doi.org/10.1021/acs.jafc.3c09106.

[31] Y. Zhou, Y. Wu, Z. Luo, et al., Regulating Reactive Oxygen Species over M–N–C Single-Atom Catalysts for Potential-Resolved Electrochemiluminescence, J. Am. Chem. Soc. 146 (2024) 12197-12205. https://doi.org/10.1021/jacs.4c02986.

[32] L.L. Li, K.P. Liu, G.H. Yang, et al., Fabrication of graphene–quantum dots composites for sensitive electrogenerated chemiluminescence immunosensing, Adv. Funct. Mater. 21 (2011) 869-878. https://doi.org/10.1002/adfm.201001550.

[33] W. Liang, M. Wang, C. Ma, J. Wang, et al., NiCo-LDH Hollow Nanocage Oxygen Evolution Reaction Promotes Luminol Electrochemiluminescence, Small 20 (2024) 2306473. https://doi.org/10.1002/smll.202306473.

[34] X. Zhang, F. Wang, Z. Li, et al., Dual-mode electrochemical/colorimetric microfluidic sensor integrated tetrahedral DNA nanostructures with Au/Ni-Co LDH NCs nanozyme for ultrasensitive detection of aflatoxin B1, Sensor. Actuat. B: Chem. 393 (2023) 134322. https://doi.org/10.1016/j.snb.2023.134322.